Letter

Analysis of fission-fragment mass distribution within the quantum-mechanical fragmentation theory

Pardeep Singh[a] and Harjeet Kaur

Department of Physics, Guru Nanak Dev University, Amritsar-143005, India

Abstract. The fission-fragment mass distribution is analysed for the $^{208}\text{Pb}(^{18}\text{O}, f)$ reaction within the quantum-mechanical fragmentation theory (QMFT). The reaction potential has been calculated by taking the binding energies, Coulomb potential and proximity potential of all possible decay channels and a stationary Schrödinger equation has been solved numerically to calculate the fission-fragment yield. The overall results for mass distribution are compared with those obtained in experiment. Fine structure dips in yield, corresponding to fragment shell closures at $Z = 50$ and $N = 82$, which are observed by Bogachev *et al.*, are reproduced successfully in the present calculations. These calculations will help to estimate the formation probabilities of fission fragments and to understand many related phenomena occurring in the fission process.

1 Introduction

Fission-fragment mass distribution is a significant observable while studying the fission process. Its characteristics become important while modelling fission-fragment yields. An asymmetry in the fission-fragment mass distribution and the ground-state deformation of the majority of nuclei were explained by adding a shell correction to the LDM deformation energy [1,2]. The interpretation of fission-fragment properties in terms of so-called fission modes [3] has been successfully applied in the actinide region [4–7].

The recent advancements in γ-γ coincidence spectroscopy of fission fragments have made it possible to measure the yield of individual pair of fragments [8,9] more precisely. This technique is applicable to both the heavy-ion fusion-fission reactions and the spontaneous fission process [10]. The pairs of correlated fission fragments also provide the information on neutron multiplicity. Using the energy conservation law, fission neutron properties can be studied theoretically. The knowledge of fission neutrons' multiplicities and their energy distributions could answer the questions about the mechanism of the fission phenomenon and the time scale of the fission process. Although the developments in the experimental techniques to measure the precise fission-fragment mass distribution are substantial, yet there is a need of a theoretical model which can calculate the formation probabilities of fission fragments to understand this phenomenon. Based

on the theory developed by Marhun and Greiner [11], the observed fission-fragment mass distribution following neutron evaporation for the $^{238}\text{U}(^{18}\text{O}, f)$ reaction [8] has been explained satisfactorily within the fragmentation theory [12].

In this paper we have analysed the $^{208}\text{Pb}(^{18}\text{O}, f)$ fission process by calculating the total reaction potential. The total reaction potential is the leftover potential of the compound nucleus which is not taken away by the fission fragments. For a more probable fission reaction, this leftover potential should be minimum. Using this potential, a stationary Schrödinger equation is solved numerically to estimate the fission-fragment yield. A description of the reaction potential and formalism to calculate the relative yields of fission fragments within the quantum-mechanical fragmentation theory (QMFT) is given in sect. 2. Results and discussion are presented in sect. 3 and finally conclusions are summarized in sect. 4.

2 Methodology and formalism

To study the $^{208}\text{Pb}(^{18}\text{O}, f)$ reaction we consider that a compound nucleus (CN) is formed in a heavy-ion fusion reaction when the ^{18}O projectile collides with the ^{208}Pb target which fissions into two fragments F_1 and F_2 along with the emission of some neutrons. Since the fission process is independent of the formation of the compound nucleus,

[a] e-mail: `pardeepphy@gmail.com`

we can write the whole process as

$$P(Z_P, N_P) + T(Z_T, N_T) \rightarrow CN(Z, N)^*$$
$$\rightarrow F_1(Z_1, N_1) + F_2(Z_2, N_2) + x\,_0^1 n. \quad (1)$$
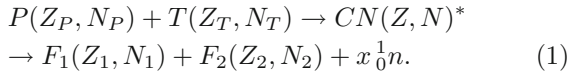
In eq. (1), x is the number of neutrons evaporated from the CN which varies from 0 to 14 in step of 2, because in the experimental study only the even-even fragments have been taken into account. When the excited and unstable CN fissions into a pair of daughter fragments and x neutrons, some part of the excitation energy of the CN is carried by the neutrons. To take care of the energy carried by the neutrons, here we introduce the concept of residual compound nucleus (RCN) and the energy of RCN must be $E^*_{RCN} = E^*_{CN} - xe_{mean}$. Here, e_{mean} is the average energy carried by neutrons [12]. After the evaporation of neutrons the RCN fissions into two fragments and this process can be shown as

$$RCN(Z, N)^* \rightarrow F_1(Z_1, N_1) + F_2(Z_2, N_2). \quad (2)$$
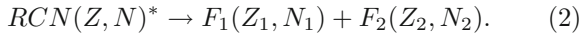
In the experiment performed by Bogachev *et al.*, it is found that the CN formed in the $^{208}\text{Pb}(^{18}\text{O}, f)$ reaction, decays into six distinct fragment pairs namely Pd-Ru, Cd-Mo, Sn-Zr, Te-Sr, Xe-Kr, and Ba-Se (see fig. 3 of ref. [9]). By taking hint from the experimental findings, we have constructed all possible correlated pairs of fission fragments by conserving the total charge, and classify them as 0, 2, 4, 6, 8, 10, 12 and 14 neutrons emission channels. To find the total reaction potential of all the decay channels, we proceed as follows.

In QMFT the dynamical collective coordinates are the mass and charge asymmetries η [$= (A_1 - A_2)/(A_1 + A_2)$] and η_z [$= (Z_1 - Z_2)/(Z_1 + Z_2)$], and R is the relative separation coordinate between the two nuclei. The total reaction potential (difference between the potential of the RCN and the potential carried by the fission fragments) can be calculated by considering the concept of RCN to take care of the energy carried by the neutrons emitted in the fission process. At a fixed value of η_z and $R = R_t$ (at touching configuration), the reaction potential can be written as

$$V(\eta) = V_{RCN} - V_F(\eta). \quad (3)$$

To calculate the potential of RCN (V_{RCN}), we have used the experimental values of the binding energies ($B.E.$) in the form of mass excess energies [13]. Products in eq. (2) consist of two fragments F_1 and F_2 and the potential involved between fragments is termed as fragmentation potential (V_F) [14] and can be calculated as

$$V_F(\eta) = -B.E.(F_1) - B.E.(F_2) + V_C + V_P. \quad (4)$$

Here, the binding energies of fragments F_1 and F_2 are also taken from ref. [13]. V_C ($= \frac{e^2 Z_1 Z_2}{R_t}$) is the Coulomb potential and V_P (calculated according to the formalism of Blocki *et al.* [15]) is the proximity potential.

By using the total potential for a particular decay channel, we have calculated the fission-fragment mass distribution for 0, 2, 4, 6, 8, 10, 12 and 14 neutron decay channel, respectively, with the help of the following method and the results are discussed in sect. 4.

2.1 Fission-fragment yield

As the compound nucleus fissions into two fragments F_1 and F_2, we can calculate the formation probability for two touching fragments described by the mass asymmetry coordinate η and their relative distance R. Considering that η motion is fast compared to R motion, R can be taken as a time-independent parameter and the stationary Schrödinger equation in η can be written as [16]

$$\left[-\frac{\hbar^2}{2\sqrt{B_{\eta\eta}}} \frac{\partial}{\partial\eta} \frac{1}{\sqrt{B_{\eta\eta}}} \frac{\partial}{\partial\eta} + V(\eta) \right] \Psi^\nu_R(\eta) = E^\nu_R \Psi^\nu_R(\eta). \quad (5)$$

We chose the value of R at a point just before the scission, by assuming that the main behavior of the distributions is already decided at this point. Once the saddle is formed, the whole system runs down the barrier. This assumption is widely used [17–20] and is supported by the constant values of the potential $V(\eta)$ and fission-fragment yields at later stages of R. The formation probability is given by the normalized yield

$$Y_0(\eta) = |\Psi_0(\eta)|^2 \sqrt{B_{\eta\eta}} \frac{2}{A}, \quad (6)$$

where the wave function $\Psi_0(\eta)$ is the ground-state solution of the stationary Schrödinger equation (5). The potential $V(\eta)$ at the touching configuration ($R = R_t$) is given by eq. (3) and the mass parameters $B_{\eta\eta}(\eta)$ are taken to be the constant mass parameters [21]. The neck degree of freedom is not included in these calculations, hence eq. (6) gives the relative yield only.

If only the ground state contributes and there is a complete adiabaticity, then $\nu = 0$. However, if the system were excited, then higher values of ν would contribute. The effects of these excitations are included through the simple Boltzmann-like occupation of excited states

$$|\Psi_R(\eta)|^2 = \frac{\sum_\nu |\Psi^\nu_R(\eta)|^2 \exp(-\frac{E^\nu_R}{\Theta})}{\sum_\nu \exp(-\frac{E^\nu_R}{\Theta})}. \quad (7)$$

Here, Θ is the nuclear temperature (in MeV) and is related to the excitation energy E^* by the following statistical expression [22]:

$$\Theta = \sqrt{\frac{10 E^*}{A}} \quad (8)$$

with $E^* = E_{cm} - Q$. In our present calculations we have taken the excitation energy $E^* = 32.5\,\text{MeV}$, corresponding to 85 MeV beam energy as taken by Bogachev *et al.* [9].

3 Results and discussion

As discussed in sect. 2, to investigate the $^{208}\text{Pb}(^{18}\text{O}, f)$ reaction we made all possible combinations for 0, 2, 4, 6, 8, 10, 12 and 14 neutrons decay channels, respectively, and calculated the reaction potential using eq. (3) for each
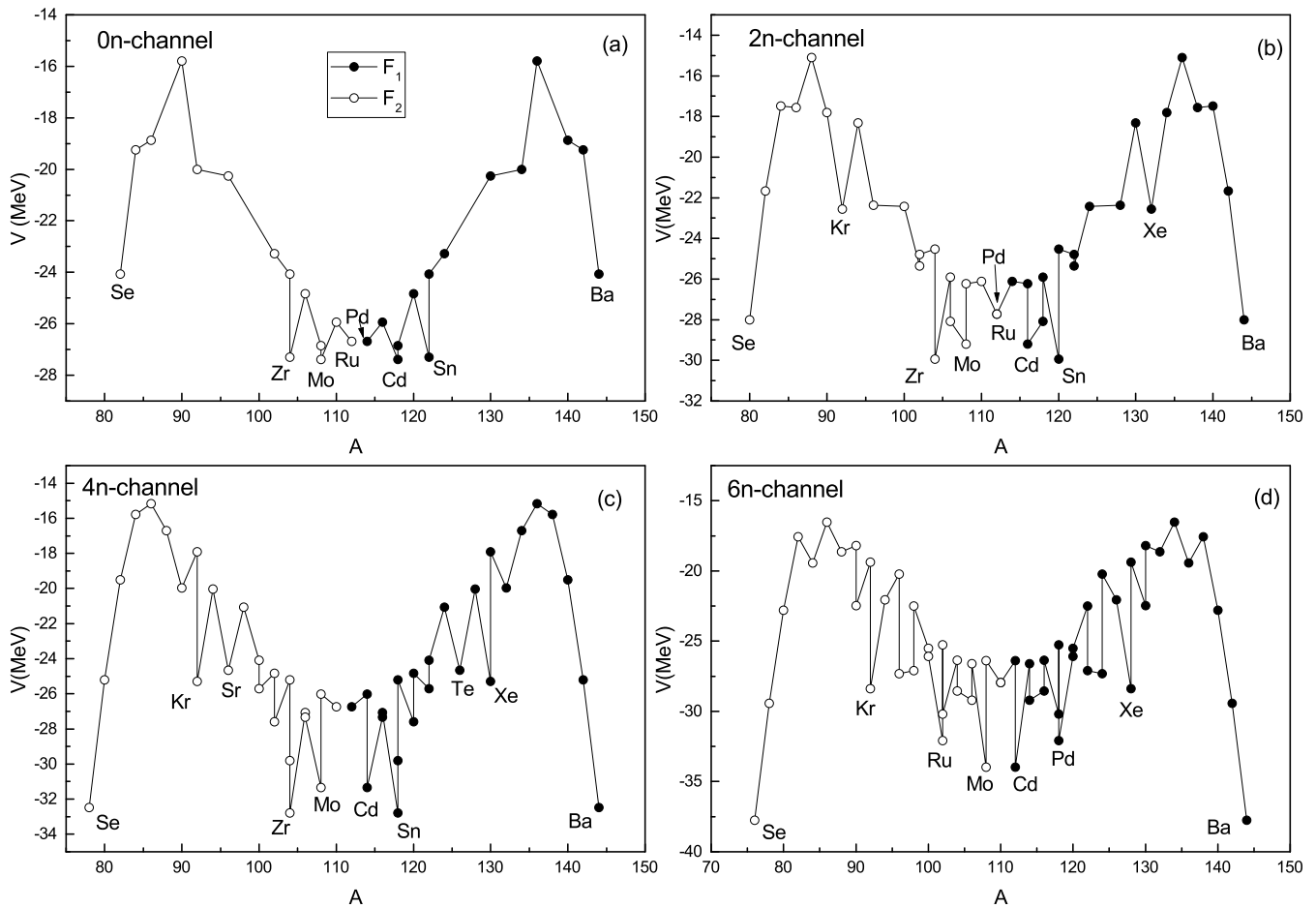
Fig. 1. Panels (a)–(d) show the potential curves for 0–6 neutron emission channels, respectively. Nuclei with higher formation probabilities (corresponding to dips in the potential curves) are also mentioned.

decay channel which is plotted against the mass numbers of the fission fragments (fig. 1(a)–(d) and fig. 2(a)–(d)). There are number of peaks and dips in the potential curves as shown in figs. 1 and 2 because of the shell effects (either in one or in both the fission fragments) which are included through the experimental binding energies. Dips correspond to the fragments with greater formation probabilities than the neighbouring fragments. The fragments with higher formation probabilities are listed in table 1, classified as 0–14 neutrons emission channels. The quadrupole deformation parameter (ϵ_2) [23] for each fission fragment is given in this table. One may notice that either one or both fission fragments have a high deformation leading to greater formation probabilities. The role of deformation has been explicitly included as we use experimental values of binding energies to determine the reaction potential $V(\eta)$ given by eq. (3). In the experiment [9], 4 and 6 neutrons emission channels have greater yields than the others and this result is in agreement with ours. From figs. 1(c) and (d) (corresponding to 4 and 6 neutrons emission channels) it is clear that the number of fragments with low reaction potential are more than those corresponding to other neutrons emission channels

and therefore these fragment pairs are more likely to form through these channels than others. Hence, 4 and 6 neutrons emission channels have higher formation probabilities than the others. Since in figs. 1(c) and (d), strong dips in potential curves are found corresponding to some isotopes of Ru-Pd and Mo-Cd, hence these isotopes have the higher formation probabilities. This result is also in agreement with the experimental findings [9].

The relative fission-fragment mass distribution is also calculated for this reaction by using eq. (6), corresponding to 0–14 neutrons emission channels separately and then the yields of the repeated fragments occurred in different channels are added to determine the total yield. The results are then plotted in fig. 3. Experimental results for the reaction ^{208}Pb(^{18}O, f) studied by Bogachev *et al.* (fig. 4 of ref. [9]) and theoretical results calculated by using the GEF code [24] at $E^* = 32.5$ MeV are also plotted in this figure. The experimental data is given on the logarithmic scale in fig. 4 of ref. [9], but for comparison we have taken the logarithm of that data and plotted it on a linear scale by normalizing it from 0 to 1. Our results show a better agrement with experimental data as compared to those produced by the GEF code. In both the plots
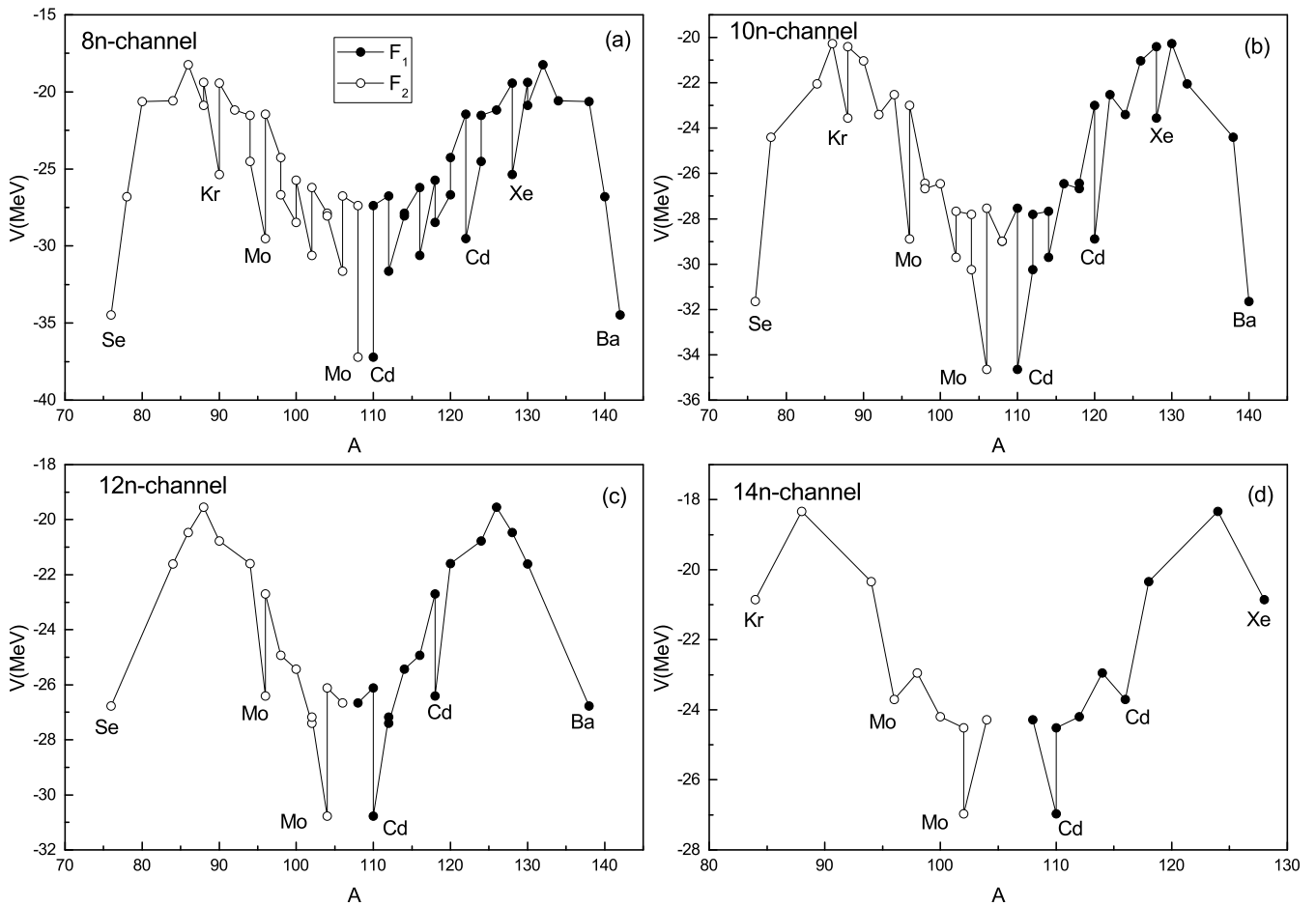
Fig. 2. Same as fig. 1 for 8–14 (panels (a)–(d), respectively) neutrons emission channels.

(experimental and our calculations), the major peak exists in the region of mass number 100–120 (around zero mass asymmetry η). We observe some dips in the mass distribution, corresponding to fragment masses $A = 82, 88, 126$ and 136, where the yield is significantly reduced. There are two major dips in the experimental plot corresponding to mass number 136 and its complementary fragment mass, which is well explained by these calculations (see fig. 3). It is most likely that the dips in the mass distribution appear because of the closed shell ($N = 82$) structure of ^{136}Xe and ^{136}Ba fragments. Moreover, Sn/Kr fragment pairs are present at the higher potential side in the potential curves (figs. 1 and 2) and have a closed shell structure of one of the fission fragment partner Sn ($Z = 50$), hence these fragments have lesser formation probabilities. The reduced yield at the shell closure can be visualised from the shape evolution of the compound nucleus from a saddle to a scission configuration and is explained as follows:

1) If one of the fission fragment of the fissioning nucleus has a closed shell configuration, its contribution to fission gets reduced as it has to overcome a relatively higher barrier in the multidimensional potential energy surface.

2) If one partner is having a closed shell configuration then it cannot be easily deformed. Hence, only the complimentary partner attains a larger deformation to proceed towards the scission configuration.

It is clear from fig. 3 that the experimental results of the fission-fragment mass distribution are reproduced successfully with some discrepancies at $A = 76, 90, 92, 94$ and 144.

4 Conclusion

The fission-fragment mass distribution of the ^{208}Pb (^{18}O, f) reaction is obtained within the QMFT. The total reaction potential is calculated by using the experimental values of the binding energies, Coulomb potential and proximity potential. Contribution of all possible fission fragments (except for fragments which correspond to the same mass asymmetry η) is included. Shell effects play a dominant role in explaining the fine structure dips in the mass distribution and are included in these calculations by the experimental values of the binding energies. As evident from fig. 3, the theoretically calculated mass distribution is in reasonable agreement with the experimental results except for few mass regions as discussed

Table 1. Most probable fission fragments in 0–14 neutron emission channels, corresponding to strong dips in the potential curves in figs. 1 and 2, along with their ϵ_2 values, are presented here.

Emission channel	F_1	ϵ_2	F_2	ϵ_2
0 neutrons	^{82}Se	0.142	^{144}Ba	0.150
	^{104}Zr	0.342	^{122}Sn	0.000
	^{108}Mo	0.300	^{118}Cd	0.233
	^{112}Ru	−0.250	^{114}Pd	−0.242
2 neutrons	^{80}Se	0.142	^{144}Ba	0.225
	^{92}Kr	0.208	^{132}Xe	0.000
	^{104}Zr	0.342	^{120}Sn	0.000
	^{98}Mo	0.167	^{116}Cd	0.233
	^{112}Ru	−0.250	^{112}Pd	−0.233
4 neutrons	^{78}Se	0.133	^{144}Ba	0.150
	^{92}Kr	0.208	^{130}Xe	−0.108
	^{96}Sr	0.308	^{126}Te	−0.100
	^{104}Zr	0.342	^{118}Sn	0.000
	^{108}Mo	0.300	^{114}Cd	0.190
6 neutrons	^{76}Se	−0.233	^{144}Ba	0.150
	^{92}Kr	0.208	^{128}Xe	0.133
	^{96}Sr	0.308	^{124}Te	−0.108
	^{102}Ru	0.175	^{118}Pd	−0.233
	^{108}Mo	0.300	^{112}Cd	0.133
8 neutrons	^{76}Se	−0.233	^{142}Ba	0.125
	^{90}Kr	0.150	^{128}Xe	0.133
	^{96}Mo	0.057	^{122}Cd	0.100
	^{108}Mo	0.300	^{110}Cd	0.133
10 neutrons	^{76}Se	−0.233	^{140}Ba	0.000
	^{88}Kr	0.058	^{128}Xe	0.133
	^{96}Mo	0.057	^{120}Cd	0.125
	^{106}Mo	0.325	^{110}Cd	0.133
12 neutrons	^{76}Se	−0.233	^{138}Ba	0.000
	^{96}Mo	0.057	^{118}Cd	−0.233
	^{104}Mo	0.317	^{110}Cd	0.133
14 neutrons	^{84}Kr	0.058	^{128}Xe	0.133
	^{96}Mo	0.057	^{116}Cd	0.233
	^{102}Mo	0.300	^{110}Cd	0.133

Fig. 3. The curve with solid circles shows the fission-fragment mass distribution calculated by combining the probabilities of 0–14 neutrons emission channels for the ^{208}Pb(^{18}O, f) fission reaction at 85 MeV ^{18}O beam energy. These results are compared with the experimental resuts (curve with hollow circles) and with those determined using GEF code (solid and dashed lines).

References

1. V. Strutinsky, Nucl. Phys. A **95**, 420 (1967).
2. V. Strutinsky, Nucl. Phys. A **122**, 1 (1968).
3. U. Brosa, S. Grossmann, A. Müller, Phys. Rep. **197**, 167 (1990).
4. P. Siegler, F.J. Hambsch, S. Oberstedt, J. Theobald, Nucl. Phys. A **594**, 45 (1995).
5. S. Oberstedt, F.J. Hambsch, F. Vivs, Nucl. Phys. A **644**, 289 (1998).
6. F. Vivs, F.J. Hambsch, H. Bax, S. Oberstedt, Nucl. Phys. A **662**, 63 (2000).
7. F.J. Hambsch, F. Vivs, P. Siegler, S. Oberstedt, Nucl. Phys. A **679**, 3 (2000).
8. L.S. Danu *et al.*, Phys. Rev. C **81**, 014311 (2010).
9. A. Bogachev *et al.*, Eur. Phys. J. A **34**, 23 (2007).
10. G.M. Ter-Akopian *et al.*, Phys. Rev. Lett. **77**, 32 (1996).
11. J.A. Maruhn, W. Greiner, Z. Phys. **251**, 431 (1972).
12. P. Singh, H. Kaur, S.S. Malik, Eur. Phys. J. A **50**, 68 (2014).
13. G. Audi *et al.*, Chin. Phys. C **36**, 1157 (2012).
14. R.K. Gupta, S. Singh, G. Münzenberg, W. Scheid, Phys. Rev. C **51**, 2623 (1995).
15. J. Blocki, J. Randrup, W. Swiatecki, C. Tsang, Ann. Phys. **105**, 427 (1977).
16. J.A. Maruhn, W. Greiner, W. Scheid, *Heavy Ion Collisions*, edited by R. Bock, Vol. **2** (North-Holland Publ. Co., 1980).

in sect. 3. The main reason for some discrepancies is that these calculations are done by using constant mass parameters ($B_{\eta\eta}$). Also, we did not include the contribution of the fragments existing at the same value of mass asymmetries (η) to reduce the time and complexity of calculations. This study will open the gate to more precise predictions of the fission-fragment yield in the fission of heavy nuclei.
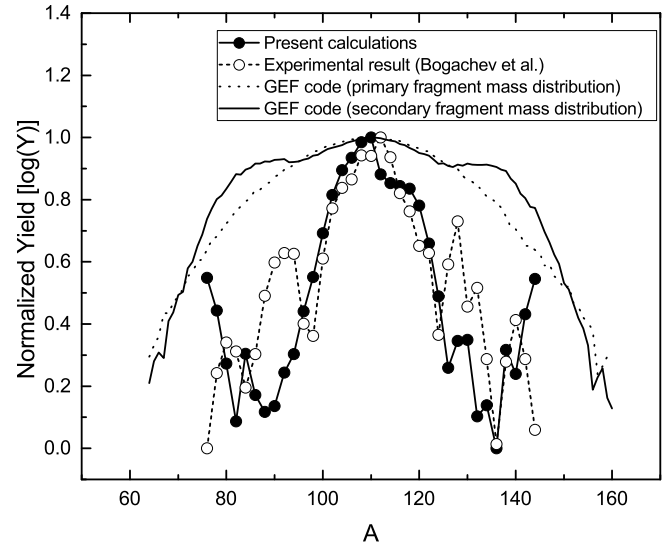
17. J. Maruhn, W. Greiner, Phys. Rev. Lett. **32**, 548 (1974).
18. R.K. Gupta, W. Scheid, W. Greiner, Phys. Rev. Lett. **35**, 353 (1975).
19. D.R. Saroha, R.K. Gupta, Phys. Rev. C **29**, 1101 (1984).
20. R.K. Gupta, D.R. Saroha, Phys. Rev. C **30**, 395 (1984).
21. H. Kroger, W. Scheid, J. Phys. G: Nucl. Phys. **6**, L85 (1980).
22. K.L. Couteur, D. Lang, Nucl. Phys. **13**, 32 (1959).
23. P. Möller, J.R. Nix, W.D. Myers, W.J. Swiatecki, At. Data Nucl. Data Tables **59**, 185 (1995).
24. K. Schmidt, B.R. Jurado, C. Amouroux, JEFF Report 24 (NEA Data Bank, June 2014).